Endoscopic cellular microscopy for *in vivo* biomechanical assessment of tendon function

Jess G. Snedeker
University and ETH Zurich
Institute for Biomedical Engineering
Zurich, Switzerland

Gadi Pelled
Yoram Zilberman
Hebrew University
Hadassah Medical Center
Skeletal Biotechnology Laboratory
Jerusalem, Israel

Friederike Gerhard
Ralph Müller
University and ETH Zurich
Institute for Biomedical Engineering
Zurich, Switzerland

Dan Gazit
Hebrew University
Hadassah Medical Center
Skeletal Biotechnology Laboratory
Jerusalem, Israel

Abstract. This study explores a novel method to quantify *in vivo* soft tissue biomechanics from endoscopic confocal fluorescence microscope images of externally loaded biological tissues. A custom algorithm based on normalized cross-correlation is used to track fluorescently labeled cells within soft tissue structures as they deform. Cellular displacements are subsequently reduced to tissue strains by deriving the spatial gradient of the spline smoothed cellular displacement field. The relative performance of the tracking method is verified using a synthetic dataset with known underlying deformation. In biological application of the method, tissue strains are measured in the Achilles tendon of an anesthetized mouse. Over repeated trials, structural strain in the tendon (i.e., the relative change in distance between cells located at view field extremes) is 20.3±3.1%, thus establishing the reproducibility of the loading protocol. Analysis of local tendon tissue strains reveal primary engineering strains in the tissue to range from 5 to 55%, signifying a highly inhomogeneous strain state, with complex relative motions of neighboring tendon substructures. In summary, the current work establishes a baseline for a promising experimental method, and demonstrates its technical feasibility. [DOI: 10.1117/1.2393153]

Keywords: biomechanics; *in vivo* soft tissue; endoscopic; cellular microscopy; fluorescence.

Paper 06107R received Apr. 27, 2006; revised manuscript received Jul. 11, 2006; accepted for publication Jul. 13, 2006; published online Dec. 4, 2006.

1 Introduction

Optical elastography, or the measurement of mechanical properties of solids using imaging techniques, is a well-established concept that takes many methodological forms.[1,2] The most classic application of using optical elastography to characterizing biological tissues is in *ex vivo* experiments, whereby simple white light videography of surface marker displacements is used to measure tissue strains while a quantified boundary load is applied. Such methods overcome practical constraints on the use of strain gages and other contact methods in quantifying large deformations in soft tissues.

Functional assessment of biological tissue mechanics is essential in proving the relative merit of novel clinical therapies for tissue healing. At present, the gold standard for biomechanical assessment is *ex vivo* mechanical testing of tissue explants. A major shortcoming of *ex vivo* biomechanical analysis is that it provides a single measurement at the conclusion of a course of treatment. Due to experimental variability, artifacts associated with tissue extraction, and intersubject variability in the response to a treatment, large numbers of subjects are typically required to verify the advantages of a given therapy over natural healing. Conversely, *in vivo* biomechanical assessment of tissue healing permits longitudinal study of regained tissue function. With such techniques, healing progress can be monitored in a single subject at various time points over the course of healing.

Various *in vivo* imaging techniques have been applied in attempt to quantify mechanical properties of tissues *in vivo*. Specifically, ultrasound[3–6] and magnetic resonance (MR) elastography[7–10] have been employed with varying degrees of success. The following study explores a novel method to quantify tissue biomechanical behavior from *in vivo* fluorescence microscopy images of cellular displacement recorded using a commercially available endoscopic confocal microscope. To the knowledge of the authors, this study describes the first application of endoscopic cellular microscopy to derive soft tissue material properties *in vivo*.

2 Methods

The method that we describe is based on the classic optical elastography paradigm: apply a quantified load, measure marker deformations, and infer the tissue strain. While the method would be generally applicable to many soft biological tissues, it is described here in the context of assessing the functional stiffness of the murine Achilles tendon. The stiffness of tendon is of primary biomechanical importance, since the tendon is responsible for the effective transmission of muscular force to the associated bone. Consequently, inappropriate tissue stiffness can result in reduced joint mobility,

Address all correspondence to Jess Snedeker, Ph.D., University and ETH Zurich, Balgrist, 340 Forchstrasse, CH-8044 Zurich, Switzerland; Tel: +41 44 386 37 55; Fax: +41 44 386 11 09; E-mail: jsnedeker@research.balgrist.ch

1083-3668/2006/11(6)/064010/8/$22.00 © 2006 SPIE

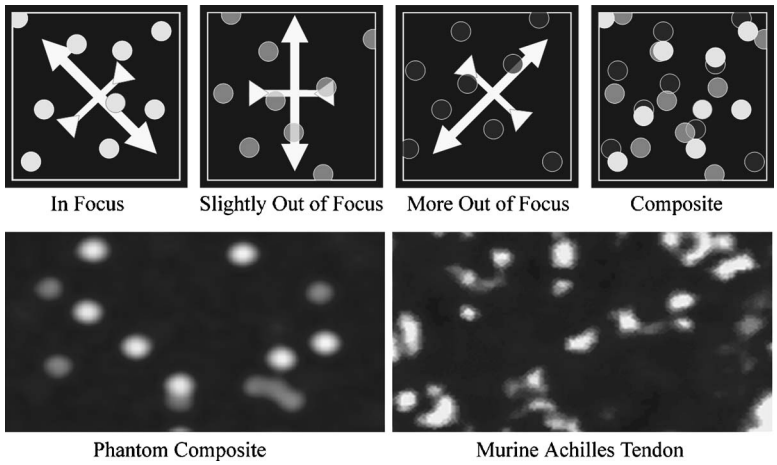

Fig. 1 Schematic representation of phantom dataset generation. Each component image represents an individual tendon substructure with a unique functional axis, with an applied tensile strain (major principal strain) on this axis and a corresponding perpendicular compressive strain (minor principal strain) due to the Poisson effect. Cells on structures that are out of focus appear with lower intensity.

pathological gait, and increased susceptibility to reinjury.[11] Thus, monitoring the stiffness of tendon over the course of a clinical therapy provides a valuable measure of regained tissue function,[12] and is a suitable example of how the proposed functional imaging method may be usefully applied.

The overall reproducibility of the method described depends on two issues: reproducibility of the tissue loading state and reliability of the displacement marker tracking. To investigate the reliability of the tracking method and to quantify effects that potential tracking errors have on measured tissue strains, a phantom dataset was synthesized. The synthetic data permit the tracking algorithms to be tested independently of experimental variability introduced by the *in vivo* tissue loading. After the potential effects of tracking error are defined, the reproducibility of the loading protocol is then investigated by comparing results from multiple *in vivo* experiments performed on an anesthetized mouse. Finally, using the validated system, the local engineering strain distribution within the murine Achilles tendon is analyzed and quantitatively described.

2.1 *Synthesis of a Benchmark Dataset*

Before application to biological datasets, a phantom dataset was synthesized to provide a benchmark for assessing the accuracy of the cellular tracking algorithms. The synthesized dataset was designed to replicate (as closely as possible) actual fluorescence endomicroscope images of displaced cells in tendons, but with a known underlying strain field.

To reproduce the influence of out-of-focus tissue structures, the dataset was generated by superimposing three reference images corresponding to cellular distributions within different tendon structures (Fig. 1). The replicated cells were modeled as disks with diameters of 6 pixels (corresponding to a cell diameter of 9 μm), and a mean intercellular spacing of 15 pixels (12 μm). Cells within each image layer were assigned fluorescence intensity according to an assumed out-of-focus distance normal to the imaging plane. The structure represented by each image layer was designated a distinct (independent) functional loading axis. The images were incrementally distorted using an affine deformation to create a series of images representing the temporal transition from an undeformed state to a fully deformed state. The deformed images of each substructure were then superimposed at coincident time points to produce a final composite image frame. The in-focus layer, corresponding to higher intensity emissions from cells in the imaging plane, was assigned a purely dilatational strain of $\varepsilon_x = -5\%$ and $\varepsilon_y = 20\%$ (strains in the local coordinate frame), with a functional loading axis rotated 45 deg counterclockwise from the vertical axis of the imaging plane. Out-of-focus layers were assigned similar strains but with the functional axis of each substructure rotated from the vertical axis by 0 and 45 deg (clockwise), respectively.

In biological tissues, local variations in tissue stiffness (for instance, tissue weakness associated with injury) are identified by subregions of high or low tissue strains. Since B-spline smoothing of the displacement field can reduce sensitivity to identifying local variations in the strain field, the capacity of the algorithm to identify such localized variation in the engineering strain field was examined. A tissue strain concentration was simulated by distorting the cellular displacement field within a designated radius of a "strain raiser" specified at a discrete point. Here, the strain concentration was designed to represent a weak spot, where the magnitude of tissue distortion is twice that of the surrounding healthy tissue. The strain profile underlying the imposed strain concentration is illustrated graphically in Fig. 2. To quantify the sensitivity of the method to local variations in the strain field, the radius of the strain concentration was progressively increased until the algorithm was able to uniquely identify it as the region of highest strain.

2.2 *Generating In Vivo Images of Cell Displacement Under a Defined External Load*

A single female C3H/HeN mouse, aged 10 weeks, was used in this study. The mouse was anesthetized using an intraperitioneally injected Ketamine-Xylazine mixture. The Achilles tendon of the right hind leg was exposed, and the cells of the tendon (tenocytes) were stained in the elastic region using SYTO 13 green fluorescent nucleic acid stain with an excita-

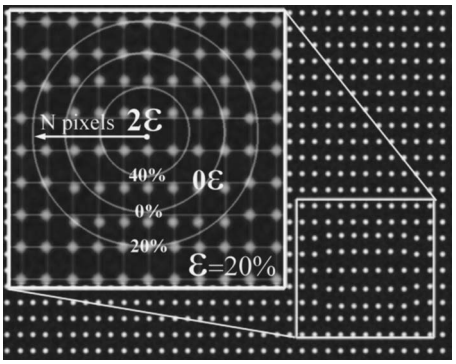

Fig. 2 Generating a local strain concentration. The "cells" shown here are distributed rectilinearly to better illustrate the imposed distortion. At the center of the defect, the tissue is stretched by a factor of two (40% maximum strain) compared to the surrounding tissue (20% maximum strain). The spatial transition from high strain to normal strain is exacted over a variable defect radius of *N* pixels.

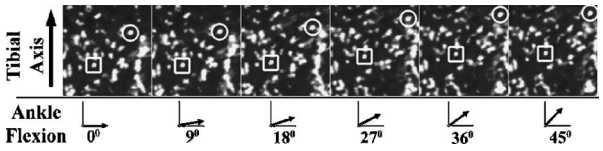

Fig. 4 Sequential images of tendon cells as the tissues are stretched by imposing an angular displacement at the ankle joint. Strains are inferred by measuring the relative change in distance between cells on the same structure.

tion wavelength of 488 nm and emission wavelength of 509 nm (Invitrogen AG, Basel, Switzerland).

The anesthetized mouse was placed in a custom loading jig (Fig. 3) that was designed and constructed to permit the application of a repeatable load to the Achilles tendon. Specifically, the femur and tibia of the mouse were physically constrained using a soft foam pad while a rotational excursion was applied at the ankle joint. As load was applied to the tendon, the relative motions of the stained tenocytes were recorded at 12 frames per second and 5-μm lateral resolution using a Cell-Vizio® S-Series endoscopic microimaging system (Mauna Kea Technologies, USA). The 650-μm objective lens at the tip of the endoscope was held in light contact with the tendon surface, and the confocal imaging depth was adjusted such that the imaging plane fell just beneath the surface of the tendon sheath. The *y* axis of the imaging plane was adjusted to align with the long axis of the tibia.

While recording movements of the tenocytes in the exposed tendon (Fig. 4), the foot was first held at a neutral posture (0 deg) and then slowly flexed from 0- to 45-deg dorsiflexion. The foot was then held at 45-deg flexion for a few seconds before being slowly returned to neutral. To investigate reproducibility, the experiment was repeated an additional four times on the same animal at five-minute intervals.

As described in the following sections, the videos of cellular movements in the imaging plane were analyzed using a cross-correlation-based tracking algorithm that extracts and derives the tissue strain field. To verify the accuracy of the algorithm, as well as the reproducibility of the tendon loading device, cell displacements and the corresponding local strains were manually determined for a readily identifiable reference tendon structure that spanned the width of the imaged field of view.

2.3 *Tracking of Cellular Displacements by Normalized Cross-Correlation*

Normalized cross-correlation (NCC) was implemented within custom software designed to track the displacements of fluorescently labeled cells over time. While the theory, merits, and shortcomings of NCC as a method for feature tracking and optical elastography are treated thoroughly in the literature,[13–17] we provide a short synopsis here for the sake of completeness and the interested reader.

Normalized cross-correlation is a robust, nonparametric method well suited for dealing with noisy image data, and is based on the block search of a grayscale pattern from one frame of a video sequence to the next. The mathematical definition of the cross-correlation coefficient $c(u,v)$ is based on a similarity measure and is given by

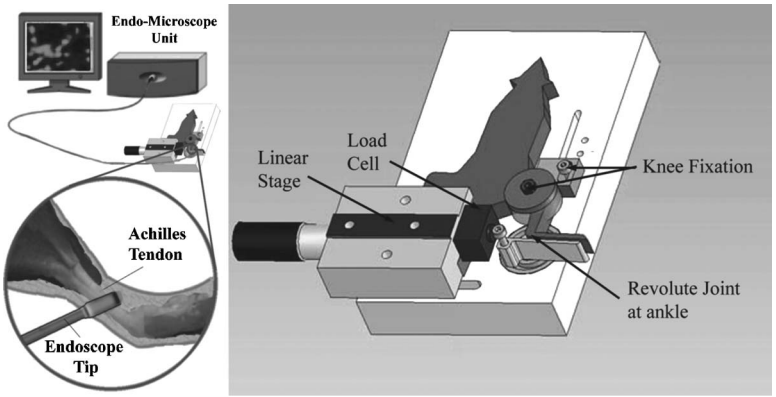

Fig. 3 Schematic representation of the experimental setup with fluorescence endomicroscope and an anesthetized mouse on the Achilles tendon stretching jig.

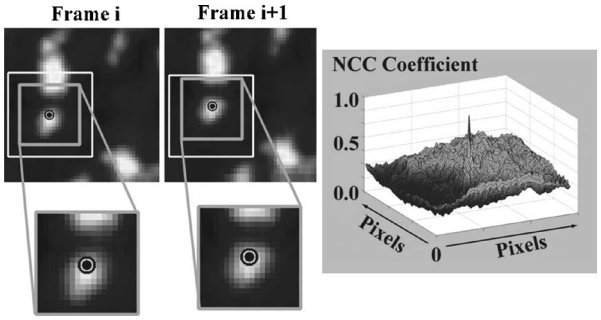

Fig. 5 Graphical representation of the principle of normalized cross-correlation. A template is created from a region of interest, including parts of several cells in frame *i*. In frame $i+1$, a search matrix (shown here as a white rectangle) is then iteratively examined to find the spatial offset of the best correlated (highest NCC coefficient) subimage match to the template. This procedure is incrementally repeated over the entire recorded sequence to determine the cumulative cellular displacement.

$$c(u,v) = \sum_{x,y} f(x,y)t(x-u,y-v), \tag{1}$$

where $f(x,y)$ is the grayscale value of the pixel with position x,y in the original block, and $t(x-u,y-v)$ is the grayscale value of the pixel with corresponding position in the shifted block. The formulation given in Eq. (1) is not invariant to fluctuations in illumination or, in the case of the present study, fluorescent dye emissions. This shortcoming is addressed by transforming (normalizing) Eq. (1) according to unit length:

$$\gamma(u,v) = \frac{\sum_{x,y}[f(x,y)-\overline{f_{u,v}}][t(x-u,y-v)-\overline{t}]}{\left\{\sum_{x,y}[f(x,y)-\overline{f_{u,v}}]^2\sum_{x,y}[t(x-u,y-v)-t]^2\right\}^{1/2}}, \tag{2}$$

where $\gamma(u,v)$ represents the degree of similarity between the reference template and the respective search pattern, and returns a value in the interval $[-1\ 1]$ for each pixel within the search area. The maximal correlation coefficient within the resulting matrix of cross-correlation values indicates the most probable displacement of the reference template from one video frame to the next.

The concept of NCC as applied to fluorescently labeled cell tracking is illustrated in Fig. 5, whereby a reference pattern of grayscale values that correspond to cells in frame *i* is to be located in frame $i+1$. After the reference template has been designated (our experience is that the template should include at least two partial cells), a search window is created in frame $i+1$ that encompasses all regions to which the template might plausibly move.

Since NCC is performed on the basis of pixel by pixel comparison, the resulting spatial resolution is limited to whole pixels. Thus, the rounding error may range up to 0.5 pixels. This error can be particularly problematic when the displacement data are later differentiated to generate tissue strain maps.[18] One way to address this issue is by subsampling (interpolating) the raw images before NCC is applied. However, increasing spatial resolution in this manner is associated with exponential increases in computational expense.

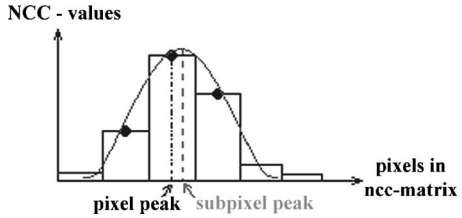

Fig. 6 1-D representation of Gaussian interpolation to determine ROI displacement with subpixel accuracy.

A computationally efficient, alternative method for attaining subpixel resolution is to instead perform the interpolation step after the cross-correlation operation has been performed.[19] Once the correlation peak is identified at whole pixel resolution, a Gaussian surface may be fitted to the correlation coefficients in the neighborhood of the whole pixel peak, and the subpixel location of the surface maximum is then used to determine the displacement of the reference template. This concept is illustrated one dimensionally in Fig. 6, and described mathematically in Eqs. (3) and (4), where u and v are the total displacement calculated with subpixel accuracy, and u_{pix} and v_{pix} are the calculated whole pixel displacements, as indicated by the peak correlation coefficient R, at pixel location i and j.

$$u = u_{\text{pix}} + \frac{\ln(R_{i-1,j}) - \ln(R_{i+1,j})}{2\ln(R_{i-1,j}) - 4\ln(R_{i,j}) + 2\ln(R_{i+1,j})}, \tag{3}$$

$$v = v_{\text{pix}} + \frac{\ln(R_{i,j-1}) - \ln(R_{i,j+1})}{2\ln(R_{i,j-1}) - 4\ln(R_{i,j}) + 2\ln(R_{i,j+1})}. \tag{4}$$

2.4 *Mapping Engineering Strains from the Cellular Displacement Field*

The ultimate goal of the method is to determine the engineering strain field of loaded soft tissues in the imaging plane. By definition, the strain field is the gradient of the deformation field, and a common approach for determining engineering strain from the displacement field relies on mapping an interpolated mathematical surface over the displacement field and calculating the spatial gradient of that surface.

In the current study, after loading the tendon and tracking the displacements of target cells, the resultant displacement field was fitted with a bicubic spline interpolated surface. As described in Eq. (5), we determine the smoothest B-spline function f that lies within a specified tolerance of the given data points $x(i)$ and $\hat{y}(i)$, where $x(i)$ are the Cartesian coordinates of cell i, and $\hat{y}(i)$ is the calculated cumulative displacement vector. To help minimize the effects of spurious displacement values, f is determined using weights assigned to each displacement data value according to its associated NCC coefficient $w(i)$. The total difference of the calculated function from the given data is measured by summing over n tracked cells.

$$E(f) = \sum_{i=1}^{n} w(i)|\{\hat{y}(i) - f[x(i)]\}|^2. \tag{5}$$

Since the image plane may not be necessarily aligned with a physiologically relevant coordinate system, tissue strains are best represented using primary and secondary (maximum and minimum) principal strains. The principal strains incorporate both dilatational strains (stretching or compression along the axes of the imaging plane) and distortional (shear) strains. Principal strain magnitudes ε_{max} and ε_{min} and direction are calculated according to Eqs. (6) through (11), where x and y represent the Cartesian coordinates of the image field, u and v represent the calculated displacement field, ε_x and ε_y are dilatational strains in the imaging plane, γ_{xy} is the shear strain in the imaging plane, and θ is the angle between the principal strain vector and the vertical axis of the imaging plane.

$$\varepsilon_x = \frac{\delta u}{\delta x}, \tag{6}$$

$$\varepsilon_y = \frac{\delta v}{\delta y}, \tag{7}$$

$$\gamma_{xy} = \frac{\delta v}{\delta x} + \frac{\delta u}{\delta y}, \tag{8}$$

$$\varepsilon_{ave} = \frac{\varepsilon_x + \varepsilon_y}{2}, \tag{9}$$

$$\varepsilon_{max,min} = \varepsilon_{ave} \pm \left\{ \left[\frac{(\varepsilon_x - \varepsilon_y)}{2} \right]^2 + \left[\frac{(\gamma_{Xy})}{2} \right]^2 \right\}^{1/2}, \tag{10}$$

$$\theta = \frac{1}{2} \mathrm{ATAN}\left(\frac{\gamma_{xy}}{(\varepsilon_x - \varepsilon_y)} \right). \tag{11}$$

3 Results

3.1 *Synthetic Benchmark Dataset*

The synthetic dataset was analyzed to isolate potential errors related to the automatic tracking of cell displacements and the subsequent mathematical reduction of displacements to tissue strains. A known strain field was imposed on the in-focus layer of the synthetic data (maximum and minimum principal strains of 20 and −5%, respectively, oriented 45% ccw to the vertical imaging axis and including a local strain concentration of peak strain 40%). The apparent strains in the phantom dataset were analyzed by deriving the spatial gradient of the displacement field as approximated by an interpolated B-spline surface.

The accuracy of the algorithm in correctly detecting the local strain field depended heavily on the degree of smoothing applied to the deformation field (Fig. 7). An optimal balance between reducing effects of spurious displacement values and maintaining sensitivity to actual differences in the local strain field was achieved with B-spline surface grid spacing set to half of the mean intercellular spacing (here 8 and 16 pixels, respectively). At this setting, the peak strain concentration (40% local strain) was uniquely identifiable as the region of highest strain, albeit with a reduced apparent magnitude (31% calculated). For a strain concentration of this magnitude, the algorithm was able to identify imposed defects of radius 2.5 times the mean intercellular spacing (i.e., 40 pixels). This equates to an experimental equivalent of 50 μm or 13% of the image field width of 600 pixels.

With this B-spline mesh grid setting, the algorithm was able to accurately assess engineering strains in regions distorted by a homogeneous strain field. The uniformly imposed maximum and minimum principal strains of 20 and −5% were determined from the local strain field to be 19.6 ± 2.5% and −5.0 ± 1.9%, respectively. The reference strain orientation of 45 deg counterclockwise from the vertical imaging axis was assessed as 46.6±1.5 deg.

3.2 *Biological Dataset*

A series of five experiments were performed on the Achilles tendon of an anesthetized mouse. *In vivo* tissue strains were inferred from endomicroscope video of tenocytes moving in response to an applied external load. Reproducibility of the tendon loading protocol was assessed using gross structural tendon strain. This structural strain was determined manually by measuring the distance between tenocytes located at distant ends of a prominent superficial tendon structure that spanned the entire field of view (as illustrated in Fig. 4). Over the five trials, manually measured engineering strain in the reference tendon structure was determined to be 20.3±3.1%, indicating that the externally induced tendon load was reproducible.

To gain insight into the heterogeneity of the local tendon strain field, tissue strains were calculated using the algorithm described in the previous sections. With algorithm settings optimized based on the results of phantom testing, the cellular deformation field was mapped using a B-spline mesh grid with a spacing of half the mean intercellular distance. Local strains estimated by the tracking algorithm ranged from 5 to 55%, indicating a highly inhomogeneous tissue strain state in the imaging plane (Fig. 8).

Cross-referencing of the cellular displacement field as tracked by the algorithm with manual inspection of the raw video confirmed that the algorithm was able to correctly track cellular displacements, indicating that the large variation in local strain did not primarily arise from tracking error. Further, visual inspection confirmed that the imaged tendon structure was complex, with both coplanar and stratified tissue substructures that alternately loaded and unloaded according to the degree of ankle rotation. While only a superficial region of the tendon was thoroughly analyzed with respect to local tissue strains, it was apparent that more superficial layers of tendon were generally stretched along the long axis of the tibia, with deeper tissue layers moving in various directions deviating from the tendon loading axis. Thus, these results revealed a complicated distribution of internal loads among the constituent structures, and indicated limitations to the assumption that all observed cells in the focal layer resided on a single structure.

4 Discussion

A novel method for *in vivo* assessment of soft tissue stiffness has been described, validated against a biofidelic synthetic dataset, and demonstrated in application to quantifying *in vivo*

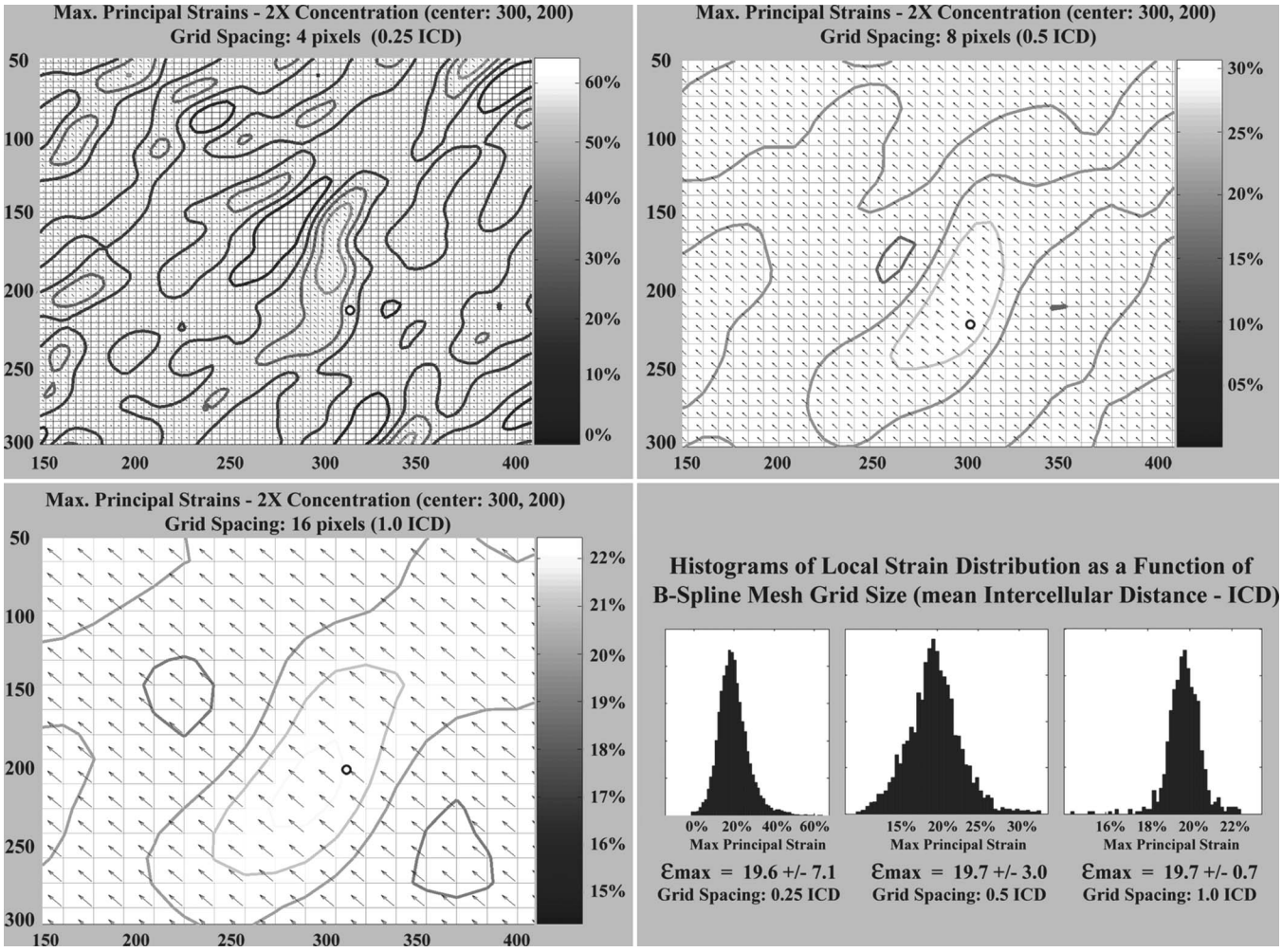

Fig. 7 Local engineering strain distributions as dependent on B-spline mesh density. Spline smoothing reduces the effects of spurious displacement values, but also reduces sensitivity in identifying real local variations in the material strain field.

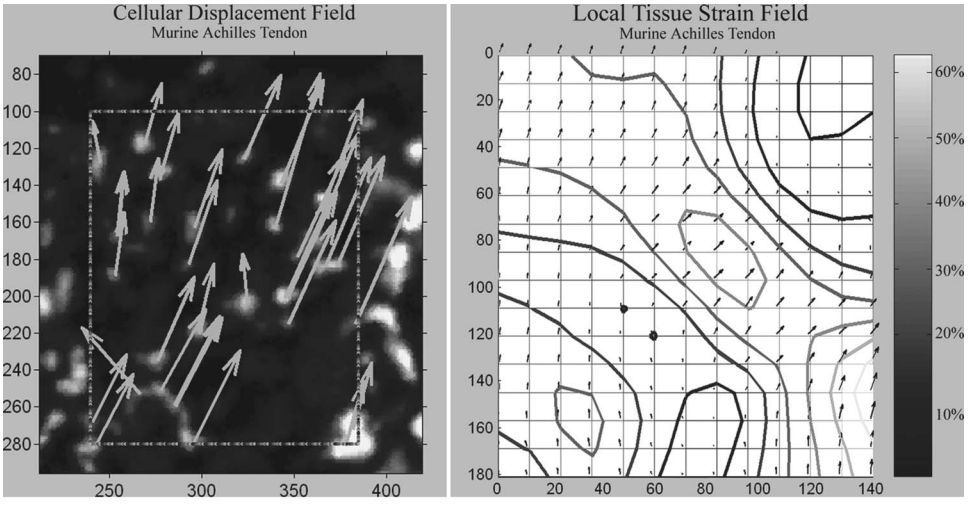

Fig. 8 (a) Full-field results of tracked 2-D cell displacements. (b) The resulting principal engineering strain distribution.

tendon strains under an applied external load. Other studies have explored optical elastography *in vivo*,[3–6] but to our knowledge, this is the first *in vivo* study examining the local strain field of a living tissue using cells as displacement markers. The ability to accurately determine the biomechanical properties of soft tissues at such high spatial resolution presents a wide and exciting range of potential applications such as examining the mechanical interactions between biological tissues and orthopedic implants, monitoring strength of tissues at injury repair sites, and performing diagnostic assessment of pathological tissue properties.

While the method shows promise, certain aspects warrant further investigation and refinement. A key limitation of the described tracking algorithm is the assumption that all cellular movements are coplanar. The Achilles tendon is composed of various substructures that work in concert to transfer force from the muscle to the bone. The functional loading axes of these substructures are not collinear and vary according to local anatomy as well as to the degree of ankle dorsi/plantar flexion and inversion/eversion. While the confocal laser endomicroscope allows one to control the tissue depth of the image plane with high precision ($\sim 15\ \mu$m), stained cells on neighboring, out-of-plane structures are faintly visible in the image field and must be excluded from consideration. A simple thresholding operation according to fluorophore emission intensity is relatively effective in restricting the number of cells being considered to those falling in the image plane. However, cells on structures that form oblique angles to the imaging plane do move into and out of the field of view over the course of the applied deformation. This effect represents a considerable source of error in the calculated strain field. Eventually, it may be possible to utilize the potential of the confocal endomicroscope to image cellular displacements in three dimensions. This information could then be implemented within more sophisticated, 3-D thresholding and/or feature tracking techniques that reduce or eliminate errors associated with a 2-D analysis.

With regard to the maximal spatial resolution of the derived engineering strain field and the sensitivity of the method in identifying local tissue defects, a sufficient volumetric concentration of cells is a limiting factor. We have therefore attempted to formulate our experiments and present our results in terms of mean intercellular spacing. This should permit the findings presented here to be applied at different levels of microscope magnification, or when labeling different types of cells of varying size.

Finally, with respect to the biological implementation of the method, it should be noted that biological tissues like tendon will exhibit different properties when stretched passively (such as by providing an external joint rotation of an anesthetized animal) compared to more biologically relevant active stretching by an excited muscle.[20,21] In future work, the isometric properties of the tendon will be examined by constraining both the ankle and the knee and actively stretching the tendon by electrode stimulation of the gastrocnemius/soleus muscle complex.

The intent of the present work was to introduce a new concept for *in vivo* biomechanical testing, describe critical technical aspects underlying the proposed method, and provide a biological example of how confocal fluorescence endomicroscopy may be used to assess *in vivo* biomechanical function of soft tissue. We do not report here on the practical utility of the method in longitudinal monitoring of tissue healing. Our ongoing work explores the applicability of the method to various animal injury models, with different clinical interventions, and observing tissue healing at discrete time points over a course of therapy.

Acknowledgments

The authors thankfully acknowledge the financial support of the European Union Integrated Project, "Adult mesenchymal stem cell engineering for connective tissue disorders. From the bench to the bed side," (GENOSTEM LSH-2003-503161). The support of the Erasmus student network (Gerhard), and the Swiss National Science Foundation (Müller) are also gratefully acknowledged.

References

1. G. L. Cloud, *Optical Methods of Engineering Analysis*, pp. xii, 503, Cambridge University Press, New York (1995).
2. D. D. Duncan and S. J. Kirkpatrick, "Processing algorithms for tracking speckle shifts in optical elastography of biological tissues," *J. Biomed. Opt.* **6**(4), 418–426 (2001).
3. J. Ophir, I. Cespedes, H. Ponnekanti, Y. Yazdi, and X. Li, "Elastography: A quantitative method for imaging the elasticity of biological tissues," *Ultrason. Imaging* **13**(2), 111–134 (1991).
4. C. Sumi, A. Suzuki, and K. Nakayama, "Estimation of shear modulus distribution in soft tissue from strain distribution," *IEEE Trans. Biomed. Eng.* **42**(2), 193–202 (1995).
5. A. R. Skovoroda, S. Y. Emelianov, and M. Odonnell, "Tissue elasticity reconstruction based on ultrasonic displacement and strain images," *IEEE Trans. Ultrason. Ferroelectr. Freq. Control* **42**(4), 747–765 (1995).
6. J. F. Greenleaf, M. Fatemi, and M. Insana, "Selected methods for imaging elastic properties of biological tissues," *Annu. Rev. Biomed. Eng.* **5**, 57–78 (2003).
7. R. Muthupillai, D. J. Lomas, P. J. Rossman, J. F. Greenleaf, A. Manduca, and R. L. Ehman, "Magnetic resonance elastography by direct visualization of propagating acoustic strain waves," *Science* **269**(5232), 1854–1857 (1995).
8. T. L. Chenevert, A. R. Skovoroda, M. O'Donnell, and S. Y. Emelianov, "Elasticity reconstructive imaging by means of stimulated echo MRI," *Magn. Reson. Med.* **39**(3), 482–490 (1998).
9. C. J. Lewa, M. Roth, L. Nicol, J. M. Franconi, and J. D. de Certaines, "A new fast and unsynchronized method for MRI of viscoelastic properties of soft tissues," *Magn. Reson. Imaging* **12**(5), 784–789 (2000).
10. K. J. Glaser, J. P. Felmlee, A. Manduca, and R. L. Ehman, "Shear stiffness estimation using intravoxel phase dispersion in magnetic resonance elastography," *Magn. Reson. Med.* **50**(6), 1256–1265 (2003).
11. S. L. Woo, R. E. Debski, J. Zeminski, S. D. Abramowitch, S. S. Saw, and J. A. Fenwick, "Injury and repair of ligaments and tendons," *Annu. Rev. Biomed. Eng.* **2**, 83–118 (2000).
12. T. C. Battaglia, R. T. Clark, A. Chhabra, V. Gaschen, E. B. Hunziker, and B. Mikic, "Ultrastructural determinants of murine achilles tendon strength during healing," *Connect. Tissue Res.* **44**(5), 218–224 (2003).
13. R. O. Duda and P. E. Hart, *Pattern Classification and Scene Analysis*, pp. xvii, 482, Wiley, New York (1973).
14. R. C. Gonzalez and R. E. Woods, *Digital Image Processing*, 2nd ed., pp. xx, 793, Prentice Hall, Upper Saddle River, NJ (2002).
15. A. Goshtasby, S. H. Gage, and J. F. Bartholic, "A 2-stage cross-correlation approach to template matching," *IEEE Trans. Pattern Anal. Mach. Intell.* **6**(3), 374–378 (1984).
16. W. K. Pratt, *Digital Image Processing*, 2nd ed., pp. xiv, 698, Wiley, New York (1991).
17. A. Svanbro, "In-plane dynamic speckle interferometry: Comparison between a combined speckle interferometry/speckle correlation and an update of the reference image," *Appl. Opt.* **43**(21), 4172–4177 (2004).

18. D. A. F. J. Quinta, P. M. Mummery, and P. J. Withers, "Full-field strain mapping by optical correlation of micrographs acquired during deformation," *J. Microsc.* **218**(1), 9–21 (2005).
19. M. Raffel, C. E. Willert, and J. Kompenhans, *Particle Image Velocimetry: A Practical Guide*, pp. xvi, 253, Springer, New York (1998).
20. C. N. Maganaris and J. P. Paul, "In vivo human tendon mechanical properties," *J. Physiol. (London)* **521**(1), 307–313 (1999).
21. C. N. Maganaris and J. P. Paul, "Tensile properties of the in vivo human gastrocnemius tendon," *J. Biomech.* **35**(12), 1639–1646 (2002).